
CMS Physics Analysis Summary

Contact: cms-pag-conveners-top@cern.ch

2022/04/10

A profile likelihood approach to measure the top quark mass in the lepton+jets channel at $\sqrt{s} = 13$ TeV

The CMS Collaboration

Abstract

The mass of the top quark is measured in 36 fb^{-1} of LHC proton-proton collision data collected with the CMS detector at $\sqrt{s} = 13$ TeV. The measurement uses a sample of $t\bar{t}$ events containing one isolated muon or electron and at least four jets in the final state. For each event, the mass is reconstructed from a kinematic fit of the decay products to a $t\bar{t}$ hypothesis. A profile likelihood method is applied to up to five observables to extract the top quark mass. The impact of systematic uncertainty sources is reduced by including their effect as nuisance parameters in the likelihood. The top quark mass is measured to be 171.77 ± 0.38 GeV.

1 Introduction

The top quark [1, 2] is the most massive known fundamental particle and its mass m_t is an important free parameter of the standard model (SM) of particle physics. Because of the large Yukawa coupling, the top quark dominates the higher-order corrections to the Higgs boson mass and a precise m_t determination allows strong constraints on the stability of the electroweak vacuum [3, 4]. In addition, precise measurements of m_t can be used to test the internal consistency of the SM [5–7].

At the CERN LHC top quarks are predominantly produced in quark-antiquark pairs ($t\bar{t}$) through the gluon fusion process and decay almost exclusively to a bottom quark and a W boson. Each $t\bar{t}$ event can be classified by the subsequent decay of the W bosons. If both decay hadronically, the final state is referred to as *all-jets* channel, if one W boson decays hadronically, and the other leptonically, the event is referred to as belonging to the *lepton+jets* channel. Event, where both W bosons decay leptonically are referred to as *di-lepton*-channel events. For this note, the lepton+jets channel is analyzed. Hence, the minimal final state consists of a muon or electron, at least four jets, and one undetected neutrino. This includes events where a muon or electron from a tau lepton decay passes the selection criteria.

The mass of the top quark has been measured with increasing precision using the invariant mass of different combinations of its decay products [8]. The measurements by the Tevatron collaborations lead to a combined value of $m_t = 174.30 \pm 0.65$ GeV [9], while the ATLAS and CMS Collaborations measured $m_t = 172.69 \pm 0.48$ GeV [10] and $m_t = 172.44 \pm 0.48$ GeV [11], respectively, from the combination of their most precise results at $\sqrt{s} = 8$ TeV (Run 1). The latter measurement achieved a relative precision on the m_t of below 0.28%. These analyses are direct top quark mass measurements that extract the m_t value from templates that are parameterized from corresponding parameter in simulation. An overview of the discussion of this mass definition and its relation to a theoretically well defined parameter is presented in [12].

In the lepton+jets channel, the top quark mass has already been measured by the CMS Collaboration with pp data at $\sqrt{s} = 13$ TeV (Run 2). Its result of $m_t = 172.25 \pm 0.63$ GeV [13] has been extracted using the ideogram method [14, 15] which has already been applied successfully in Run 1 [11]. In contrast to the Run 1 analysis, the renormalization and factorization scales in the matrix-element (ME) calculation and the scales in the initial- and final-state parton showers (PS) have been varied separately for the evaluation of systematic effects. In addition, the impact of extended models of color reconnection that were not available for the Run 1 measurements have been evaluated. The latter has lead to an increase in the systematic uncertainty [13].

In this publication we employ an improved mass extraction method on the same data as used in Ref. [13]. In addition to the improvements in the mass extraction technique, the reconstruction and calibration of the analyzed data have been improved and updated simulations are used. For example the underlying event tune CP5 [16] and the bottom flavor jet tagger DEEPJET [17] were not available in the former analysis on the same data. The analysis employs a kinematic fit of the decay products to a $t\bar{t}$ hypothesis. For each event only the assignment of the jets to the decay products that matches the hypothesis best, is used. A profile likelihood fit is performed to up to five different observables to constrain the main systematic uncertainty sources. The model for the likelihood incorporates the effects of variations of these sources represented by nuisance parameters based on simulation as well as the limits of the simulated statistic on these variations. This reduces the influence of systematic uncertainties on the measurement.

2 Data samples and event selection

The analyzed data sample has been collected with the CMS detector during the data taking period in 2016 at a center-of-mass energy $\sqrt{s} = 13$ TeV. It corresponds to an integrated luminosity of 36 fb^{-1} [18]. Events are required to pass a single-muon trigger with a minimum threshold on the p_T of an isolated muon of 24 GeV or a single-electron trigger with a p_T threshold for isolated electrons of 27 GeV [19].

Simulated $t\bar{t}$ signal events were generated with the POWHEG v2 matrix-element (ME) generator [20–22] and PYTHIA 8.219 parton showering (PS) [23, 24] and used the CP5 underlying event tune [16] with top quark mass values m_t^{gen} of 169.5, 172.5 and 175.5 GeV. To model parton distribution functions (PDF) the NNPDF3.1 NNLO set [25–27] is used with the strong coupling constant α_s set to $\alpha_s = 0.118$. The various background samples were simulated with the same ME generators and matching techniques [28–32] as in Ref. [13]. The PS simulation and hadronization was performed with PYTHIA 8 using the CUETP8M1 tune [33].

All simulated samples were processed through a full simulation of the CMS detector based on GEANT4 [34] and are normalized to their predicted cross-section described in Refs. [35–39]. Effects of additional interactions per bunch crossing (pileup) are included in the simulation and weighted to match the distribution in data. The jet energy response and resolution in simulated events is corrected to match the measured events [40]. In addition the b-jet identification (b tagging) efficiency and misidentification rate and the lepton trigger and reconstruction efficiencies are corrected in simulation.

Events with exactly one isolated muon (electron) with $p_T > 26$ (29) GeV, $|\eta| < 2.4$ are selected that are isolated from particle-flow jet candidates within $\Delta R = \sqrt{\Delta\eta^2 + \Delta\phi^2} < 0.4$ (0.3), where $\Delta\eta$ and $\Delta\phi$ are the difference in pseudorapidity and azimuthal angles between the jet and lepton candidate. The four leading jet candidates of each event are required to have $p_T > 30$ GeV and $|\eta| < 2.4$. Only these four jets are used in the further reconstruction. Jets origination from b quarks are identified using the DEEPIET algorithm [17, 41]. For jets from $t\bar{t}$ simulation in the *all-jets* decay channel with $p_T > 30$ and $|\eta| < 2.5$ it has an efficiency of approximately 78% at a mistagging probability for light-quark and gluon jets of 1% [17, 41]. Exactly two b-tags are required in the four selected jets, selecting 451 618 (287 842) candidate events of $t\bar{t}$ decaying into one muon or electron and jets.

To check the compatibility of an event with the $t\bar{t}$ hypothesis, and to improve the resolution of the reconstructed quantities, a kinematic fit [42] is performed. For each event, the inputs to the algorithm are the four-momenta of the lepton and of the four leading jets, \vec{p}_T^{miss} , and the resolutions of these variables. The fit constrains these quantities to the hypothesis that two heavy particles of equal mass are produced, each one decaying to a bottom quark and a W boson, with the invariant mass of the latter constrained to 80.4 GeV. The kinematic fit then minimizes $\chi^2 \equiv (\mathbf{x} - \mathbf{x}^m)^T G (\mathbf{x} - \mathbf{x}^m)$ where \mathbf{x}^m and \mathbf{x} are the vectors of the measured and fitted momenta, respectively, and G is the inverse covariance matrix which is constructed from the uncertainties in the measured momenta. The two b-tagged jets are candidates for the b quarks in the $t\bar{t}$ hypothesis, while the two jets that are not b-tagged serve as candidates for the light quarks from the hadronically decaying W boson. This leads to two possible parton-jet assignments with two solutions for the longitudinal component of the neutrino momentum each, resulting in four different permutations per event. For simulated $t\bar{t}$ events, the parton-jet assignments can be classified as correct permutations, wrong permutations, and unmatched permutations, where, in the latter, at least one quark from the $t\bar{t}$ decay is not unambiguously matched within a distance of $\Delta R < 0.4$ to any of the four selected jets.

The goodness-of-fit probability $P_{\text{gof}} = \exp(-\frac{1}{2}\chi^2)$ is used to determine the most likely jet-parton assignment. For each event, the observables from the permutation with the highest goodness-of-fit probability are the input to the m_t measurement. In addition the events are categorized in $P_{\text{gof}} < 0.2$ and $P_{\text{gof}} \geq 0.2$. The latter category contains 140 362 (87 265) $t\bar{t}$ candidate events in the *lepton+jets* decay channel with a predicted signal fraction of 95% improving the fraction of correctly reconstructed events from 20% to 47%. Figure 1 shows the distribution of the invariant mass of the hadronically decaying top quark candidate before and after the $P_{\text{gof}} \geq 0.2$ selection and the kinematic fit. Albeit the simulation predicts in all distributions 10% more events, the normalization of the simulation agrees within the uncertainties. For the final measurement, the simulation is normalized to the number of events observed in data.

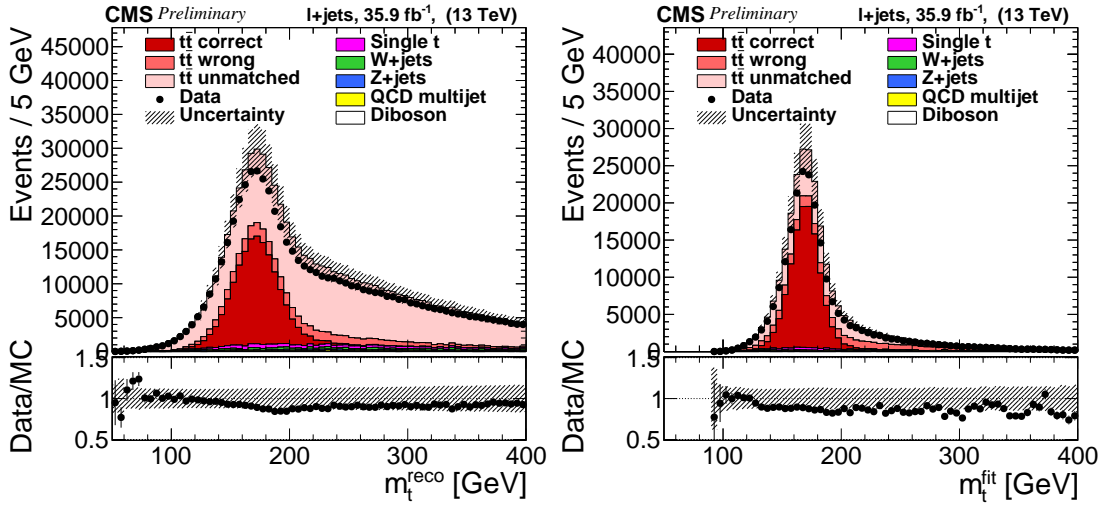


Figure 1: The top quark mass distribution before (left) and after (right) the $P_{\text{gof}} \geq 0.2$ selection and the kinematic fit. For the simulated $t\bar{t}$ events, the jet-parton assignments are classified as correct, wrong, and unmatched permutations as described in the text. The uncertainty bands contain statistical uncertainties in the simulation, normalization uncertainties due to luminosity and cross-section, and all weight-based uncertainties. A value of $m_t^{\text{gen}} = 172.5 \text{ GeV}$ is used in the simulation.

3 Observables and systematic uncertainties

For events with $P_{\text{gof}} \geq 0.2$, the mass of the top quark candidates from the kinematic fit m_t^{fit} shows a very strong dependence on m_t and is the main observable in this analysis. For events with $P_{\text{gof}} < 0.2$, the invariant mass of the lepton and the b-tagged jet assigned to the semileptonic decaying top quark $m_{\ell b}^{\text{reco}}$ is shown in Fig.2 right. For most $t\bar{t}$ events a low P_{gof} value is caused by assigning the wrong jets to the W boson candidate while the two b-tagged jets are the correct candidates for the b quarks. Hence, $m_{\ell b}^{\text{reco}}$ preserves a good m_t dependence and adds additional sensitivity to the measurement. It is new to the CMS top quark mass measurements in the lepton+jets channel, but a similar observable has routinely been used in top mass measurement in the di-lepton channel [43, 44].

Additional observables are used in parallel for the mass extraction to constrain systematic uncertainties. The invariant mass of the two untagged jets before the kinematic fit m_W^{reco} has been used together with m_t^{fit} in previous CMS analyses in the lepton+jets channel mainly to reduce the uncertainty on the jet energy scale and the jet modeling. Its distribution is shown in Fig.2

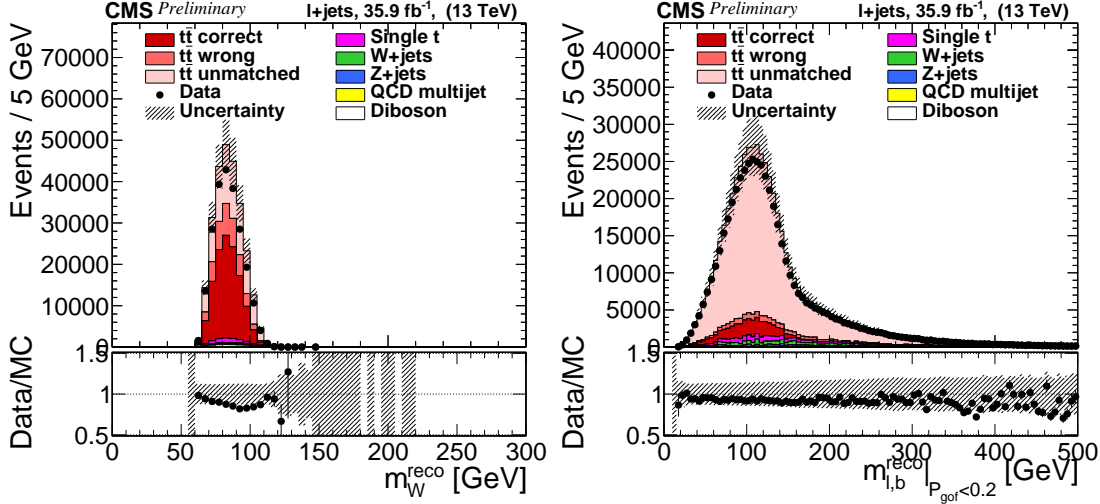


Figure 2: The distributions of the reconstructed W boson mass for the $P_{\text{gof}} \geq 0.2$ category (left) and of the invariant mass of the lepton and the jet assigned to the semileptonic decaying top quark for the category $P_{\text{gof}} < 0.2$ category (right). The uncertainty bands contain statistical uncertainties in the simulation, normalization uncertainties due to luminosity and cross-section, and all weight-based uncertainties. A value of $m_t^{\text{gen}} = 172.5 \text{ GeV}$ is used in the simulation.

left. As m_W^{reco} is only sensitive to the energy scale and modeling of light flavor jets, two additional observables are employed to improve sensitivity on the scale and modeling of jets originating from b quarks. These are the ratio $m_{\ell b}^{\text{reco}}/m_t^{\text{fit}}$, and the ratio of the scalar sum of the transverse momenta of the two b-tagged jets (b1, b2), and the two untagged jets (q1, q2) $R_{\text{bq}}^{\text{reco}} = (p_T^{b1} + p_T^{b2})/(p_T^{q1} + p_T^{q2})$. Their distributions are shown in Fig.3. While m_t^{fit} and m_W^{reco} have been used in previous CMS analyses in the lepton+jets channel, $m_{\ell b}^{\text{reco}}$, $m_{\ell b}^{\text{reco}}/m_t^{\text{fit}}$, and $R_{\text{bq}}^{\text{reco}}$ are a new addition. However, $R_{\text{bq}}^{\text{reco}}$ has been used in the lepton+jets channel by the ATLAS Collaboration [10, 45].

The distributions of the five observables are affected by uncertainties on the modeling and the reconstruction of the simulated events. These sources of systematic uncertainties on this measurement are identical to the previous results [13, 46]. They can be summarized in the following categories.

- *Calibration*: The statistical uncertainty on the top quark mass dependence due to limited size of the simulated samples for different m_t^{gen} is included via nuisance parameters in the likelihood.
- *Jet energy correction (JEC)* Jet energies are scaled up and down according to the p_T - and η -dependent data/simulation uncertainties [40]. Each of the 25 individual uncertainties on the jet energy corrections is represented by its own nuisance parameter.
- *Jet energy resolution (JER)*: Since the jet energy resolution measured in data is worse than in simulation, the simulation is modified to correct for the difference [40]. The jet energy resolution in the simulation is varied up and down within the uncertainty. The variation is evaluated independent for two $|\eta_{\text{jet}}|$ regions, split at $|\eta_{\text{jet}}| = 1.93$.
- *b tagging*: The p_T -dependent uncertainty of the b tagging efficiencies and misidentification rates of the DEEPJET b tagger [17, 41] are taken into account by weighting the simulated events.

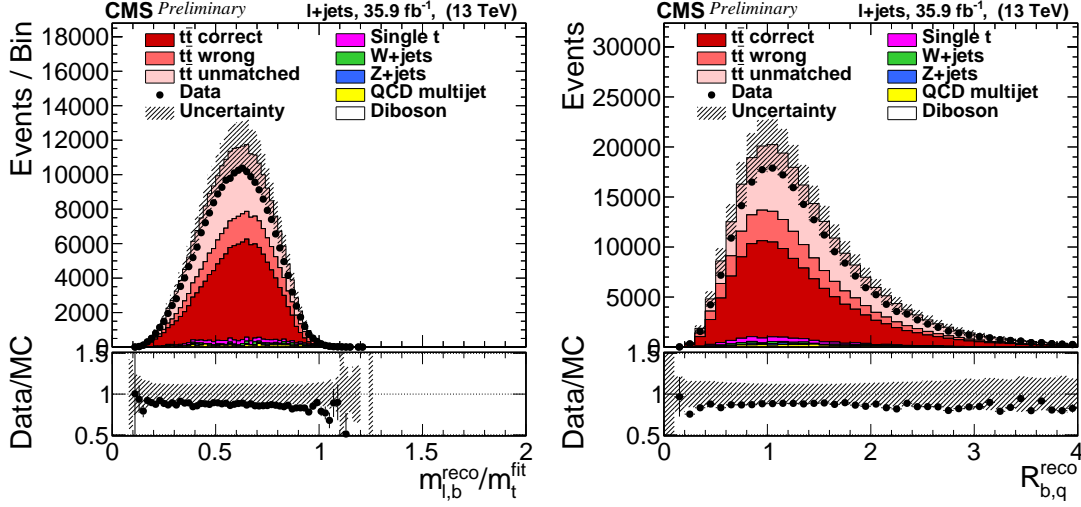


Figure 3: The distributions of m_{lb}^{reco}/m_t^{fit} , the invariant mass of the lepton and the jet assigned to the semileptonic decaying top quark divided by the top quark mass from the kinematic fit, (left) and of $R_{b,q}^{reco}$, the ratio of the scalar sum of the transverse momenta of the two b-tagged jets, and the two leading untagged jets (right), both for the $P_{gof} \geq 0.2$ category. The uncertainty bands contain statistical uncertainties in the simulation, normalization uncertainties due to luminosity and cross-section, and all weight-based uncertainties. A value of $m_t^{gen} = 172.5 \text{ GeV}$ is used in the simulation.

- *Pileup*: To estimate the uncertainty from the determination of the number of pileup events and the reweighting procedure, the inelastic proton-proton cross section [47] used in the determination is varied by $\pm 4.6\%$.
- *Background (BG)*: The main uncertainty in the non- $t\bar{t}$ background stems from the uncertainty in the measurements of the cross sections used in the normalization. The normalization of the background samples is varied by $\pm 10\%$ for the single top quark samples [48, 49], $\pm 30\%$ for the W+jets samples [50], $\pm 10\%$ for the Z+jets [51] and for the diboson samples [52, 53], and $\pm 100\%$ for the QCD multijet samples. The uncertainty in the luminosity of 2.5% [18] is negligible compared to these variations.
- *Electron and Muon scale factors (SFs)*: The simulation to data scale factors for the trigger, reconstruction, and selection efficiencies for electrons or muons are varied simultaneously within their uncertainties.
- *Lepton momentum corrections*: The lepton energy in simulation is varied up and down by one standard deviation of its energy correction.
- *JEC flavor*: The difference between Lund string fragmentation and cluster fragmentation is evaluated comparing PYTHIA 6.422 [23] and HERWIG++ 2.4 [54]. The jet energy response is compared separately for each jet flavor [40].
- *b jet modeling (bJES)*: The uncertainty associated with the fragmentation of b quarks is split into four components. The Bowler-Lund fragmentation function is varied symmetric within its uncertainties as determined by the ALEPH and DELPHI Collaborations [55, 56]. The difference between the default PYTHIA setting and the center of the variations is included as additional uncertainty. As an alternative model of the fragmentation into b hadrons, the Peterson fragmentation function is used and the difference obtained relative to the Bowler-Lund fragmentation function is assigned as an uncertainty. The third uncertainty source taken into account is the

semileptonic b hadron branching fraction, which is varied by -0.45% and $+0.77\%$, motivated by measurements of B^0/B^+ decays and their corresponding uncertainties [8].

- *Parton distribution function (PDF)*: The default NNPDF3.1 NNLO [25–27] is compared to the CT14 NNLO [57] and MMHT 2014 NNLO [58] PDFs via event weights. In addition, the α_s value is varied to 0.117 and 0.119 in the default set. A variation of the default PDF with 100 Hessian eigenvectors was found to be negligible on the final result and is not included in the presented measurement.
- *Renormalization and factorization scales*: The renormalization and factorization scales for the ME calculation are varied. Both are varied independently by a factor of two. This is achieved by appropriately reweighting simulated events. Only the simultaneous change is introduced as a nuisance parameter as it covers the effects of the two other variations.
- *ME to PS matching*: The matching of the POWHEG ME calculations to the PYTHIA PS is varied by shifting the parameter $h_{\text{damp}} = 1.58^{+0.66}_{-0.59}$ [59] within the uncertainties.
- *ISR and FSR*: For initial-state radiation (ISR) and final-state radiation (FSR), 32 decorrelated variations of the renormalization scale and non-singular terms (cNS) for each branching type ($g \rightarrow gg$, $g \rightarrow qq$, $q \rightarrow qg$, and $X \rightarrow Xg$ with $X = t$ or b) are applied using event weights [60]. The scale variations correspond to a change of the respective PS scale in PYTHIA by factors of 2 and 1/2. This approach is new compared to the previous analysis [13] which evaluated only correlated changes in the FSR and ISR PS scales. The dependence on the FSR PS scale variation is parameterized with a second order polynomial.
- *Top quark p_T* : Recent calculations suggest that the top quark p_T spectrum is strongly affected by next-to-next-to-leading-order effects [61–63]. The p_T of the top quark in simulation is varied to match the distribution measured by CMS [64, 65] and this variation is included via a nuisance parameter in the m_t measurement.
- *Underlying event (UE)*: Measurements of the underlying event have been used to tune PYTHIA parameters describing nonperturbative QCD effects [16, 33]. The parameters of the tune are varied within their uncertainties.
- *Early resonance decays (ERD)*: Modeling of color reconnection (CR) introduces systematic uncertainties which are estimated by comparing different CR models and settings. In the default sample, the top quark decay products are not included in the CR process. This setting is compared to the case of including the decay products by enabling early resonance decays in PYTHIA 8.
- *CR modeling*: In addition to the default model used in PYTHIA 8, two alternative CR models are used, namely a model with string formation beyond leading color (“QCD inspired”) [66] and a model allowing the gluons to be moved to another string (“gluon move”) [67]. Underlying event measurements are used to tune the parameters of all models [16]. Each model is represented by an individual continuous nuisance parameter. So the nuisance parameters can correspond to a mixing of the CR models.

4 Mass extraction method

A maximum likelihood (ML) fit to the recorded data is employed to measure m_t . The evaluated likelihood ratio $\lambda(m_t, \vec{\theta}, \vec{\beta}, \vec{\omega} | \text{data})$ depends not only on m_t , but also on three sets of nuisance

parameters. The nuisance parameters $\vec{\theta}$ incorporate the uncertainty on systematic effects into the measurement, while the *statistical* nuisance parameters $\vec{\beta}$ and $\vec{\omega}$ account for the statistical uncertainties on the simulation. For the nuisance parameters, a value of 0 represents the absence of the systematic effect and the values ± 1 correspond to a variation of the systematic effect by one standard deviation up or down. The ROOFIT [68] package is used to define and evaluate all the functions. The minimum of the negative log-likelihood $-2 \ln \lambda(m_t, \vec{\theta}, \vec{\beta}, \vec{\omega} | \text{data})$ is found with the MINUIT2 package [69].

The data are characterized by the five observables per event mentioned above. The events are split into the electron+jets and the muon+jets channel. The input to the maximum likelihood fit is a set of one dimensional histograms of the observables in certain categories. Different sets of histograms are investigated to evaluate their impact on the precision of the mass measurement. The probability density function $P(\text{data} | m_t, \vec{\theta}, \vec{\beta}, \vec{\omega})$ is simplified to $P(\text{data} | m_t, \vec{\theta}, \vec{\beta}, \vec{\omega}) = \prod_i P_i(x_i | m_t, \vec{\theta}, \vec{\beta}, \vec{\omega})$ where x_i iterates over all observables used in a specific set. This simplification works as all observables are independent in most phase space regions and has been verified with pseudo-experiments on simulation and data.

For a single histogram in a set with the observable x_i , the bin contents $n_{i,j}$ with bin center $x_{i,j}$, and the total number of entries n_{tot} the likelihood ratio λ_i of products of Poisson probabilities for the prediction $\mu_{i,j} = n_{\text{tot}} P(x_{i,j} | m_t, \vec{\theta}, \vec{\beta}, \vec{\omega})$ and the Poisson probabilities for a model with adjustable parameters per bin $\hat{\mu}_{i,j} = n_{i,j}$ [8] are used. Then the combined likelihood ratio for a set with observables \vec{x} is

$$\lambda(m_t, \vec{\theta}, \vec{\beta}, \vec{\omega} | \text{data}) = \left(\prod_i \lambda_i(m_t, \vec{\theta}, \vec{\beta}, \vec{\omega} | x_i) P(\vec{\beta}) P(\vec{\omega}) \right) \left(\prod_l P(\theta_l) \right),$$

where $P(\theta)$, $P(\vec{\beta})$, and $P(\vec{\omega})$ are the pre-fit probability density functions of the nuisance parameters $\vec{\theta}$, $\vec{\beta}$, and $\vec{\omega}$. The probability density functions of the nuisance parameters related to systematic uncertainties $P(\theta_l)$ are standard normal distributions. The *statistical* nuisance parameters $\vec{\beta}$ and $\vec{\omega}$ are constrained by centered multivariate normal distributions where their covariance matrices are taken from the fit of the model parameters. The latter nuisance parameters and constraints are only included if the model parameters are determined on samples that are statistically independent to the default simulation. If the model parameters are determined on samples obtained from weighting the default simulation and, hence, the statistical uncertainties on the respective model parameters are very small, the corresponding ω parameters are fixed to zero and the constraint is removed from $\lambda(m_t, \vec{\theta}, \vec{\beta}, \vec{\omega} | \text{data})$.

The probability density function for the m_t^{fit} histograms is approximated by the sum of a Voigt profile (convolution of a Cauchy-Lorentz distribution and a Gaussian distribution) for the correctly reconstructed $t\bar{t}$ candidates and Chebyshev polynomials [70] for the remaining events. For all other observables a binned probability density function is used. Here, eight bins are used for each observable and the width of the bins is chosen so that each bin has a similar number of selected events for the default simulation ($m_t^{\text{gen}} = 172.5 \text{ GeV}$). For the following, we denote the parameters of the probability density functions as \vec{a} . All the functions are normalized to the number of events in the histogram, so only shape information is used in the ML fit. Hence, the parameters \vec{a} are correlated even for the binned probability density function. The dependence of these parameters on m_t and $\vec{\theta}$ is assumed to be linear. The full expression is for

a component α_k of $\vec{\alpha}$

$$\alpha_k = C_k \cdot \left(1 + d_k \cdot \left(\alpha_k^0 + \beta_k + s_k^0 \cdot (m_t - 172.5 \text{ GeV}) + \omega_k^0 \cdot 1 \text{ GeV} \right) \right) \times \prod_l \left(1 + d_k \cdot \left(s_k^l \cdot \theta_l + \omega_k^l \cdot 1 \right) \right), \quad (1)$$

with k indicating the parameter of the observables probability density function and l indicating the nuisance parameter. For the nuisance parameters corresponding to the FSR PS scale variations, the linear term, $s_k^l \cdot \theta_l$, is replaced with a second order polynomial. The model parameter α_k^0 is determined by a fit to the default simulation, while the linear dependencies of α_k on m_t or a component θ_l of $\vec{\theta}$ are expressed with the model parameters s_k^0 and s_k^l respectively. The parameter s_k^0 is determined by a simultaneous fit to simulations where m_t^{gen} is varied by $\pm 3 \text{ GeV}$ from the default value. Along the same lines, the parameters s_k^l are obtained from fits to the simulation of the systematic effect corresponding to the nuisance θ_l . The values of C_k and d_k are chosen ad-hoc so that the results of the fits of α_k^0 , s_k^0 , and the s_k^l are all of the same order of magnitude and with a similar statistical uncertainty. This improves the numerical stability of the final ML fit. The limited sample size on the simulations for different m_t^{gen} values gives rise to a calibration uncertainty on m_t . Hence, additional *statistical* nuisance parameters β_k , ω_k^0 are introduced that account for the statistical uncertainty on the model parameters α_k^0 , s_k^0 . Similarly, the parameters s_k^l contain random fluctuations if they are determined on simulations that are statistically independent to the default simulation and of limited size. These fluctuations can lead to overconstraints on the corresponding nuisance parameters and, hence, an underestimation of the systematic uncertainty. The nuisance parameters ω_k^l are added to counter these effects. As mentioned above, the $\vec{\beta}$ and $\vec{\omega}$ nuisance parameters are constrained in the ML fit by multivariate normal distributions to take the correlations between the parameters into account.

The mass of the top quark is determined with the profile likelihood fit for different sets of data histograms. The sets and their labels are listed in Table 1.

Table 1: The overall list of different input histograms and their inclusion in a certain histogram set. A histogram marked with "x" is included in a set (measurement).

histogram		set label				
observable	category	1D	2D	3D	4D	5D
m_t^{fit}	$P_{\text{gof}} \geq 0.2$	x	x	x	x	x
m_W^{reco}	$P_{\text{gof}} \geq 0.2$		x	x	x	x
$m_{\ell b}^{\text{reco}}$	$P_{\text{gof}} < 0.2$			x	x	x
$m_{\ell b}^{\text{reco}} / m_t^{\text{fit}}$	$P_{\text{gof}} \geq 0.2$				x	x
R_{bq}^{reco}	$P_{\text{gof}} \geq 0.2$					x

The expected total uncertainty on m_t is evaluated for each set defined in Table 1 with pseudo-experiments using the default simulation. The results of the pseudo-experiments are shown in Fig. 4 (left). The improvements in the data reconstruction and calibration, event selection, simulation, and mass extraction method result in a reduction for the *1D* measurement from 1.09 GeV to 0.64 GeV when compared to the previous measurement [13]. The *2D* measurement improves from 0.62 GeV to 0.50 GeV. The additional observables and the split into categories further reduces the expected uncertainty down to 0.37 GeV for the *5D* set.

The statistical uncertainty is obtained from fits that only have m_t as a free parameter. It is expected to be 0.07, 0.06, and 0.04 GeV in the electron+jets, muon+jets, and lepton+jets channels,

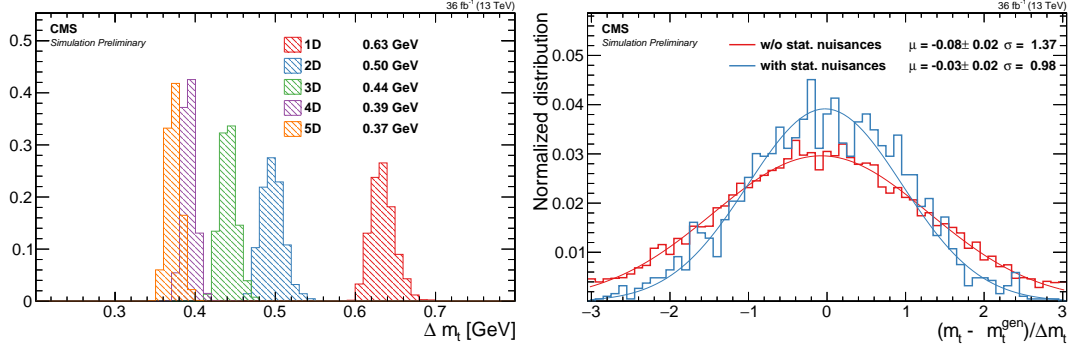


Figure 4: Left: Comparison of the expected total uncertainty on m_t in the combined lepton+jets channel and for the different observable-category sets defined in Table 1.

Right: The difference between the measured and generated m_t values divided by the uncertainty reported by the fit from pseudo-experiments without (red) or with (blue) the *statistical* nuisance parameters $\vec{\beta}$ and $\vec{\omega}$ in the ML fit. The μ and σ parameters of Gaussian functions (red and blue lines) fit to the histograms are included in the legend.

respectively.

The applied statistical model is verified with additional pseudo-experiments. The data for one pseudo-experiment is generated using probability density functions $P(x_{i,j}|m_t, \vec{\theta})$ that have the same functional form as the ones used in the ML fit, but their model parameters $\vec{\alpha}$ and $\vec{\gamma}$ are determined on statistically fluctuated simulations. For the generation of a pseudo-experiment, m_t is chosen randomly between $172.5 - \sqrt{3}$ and $172.5 + \sqrt{3}$ GeV, while the values of the nuisance parameters $\vec{\theta}$ are drawn from standard normal distributions. The same ML fit as applied to the collider data is then performed on the pseudo-data. The pseudo-experiments are performed for two cases, i.e., with and without the *statistical* nuisance parameters $\vec{\beta}$ and $\vec{\omega}$ in the ML fit. Fig. 4 (right) shows the distribution of the differences between the measured and generated m_t values divided by the uncertainty reported by the fit for both cases. A nearly 40% underestimation of the measurement uncertainty can be seen for the case without the *statistical* nuisance parameters $\vec{\beta}$ and $\vec{\omega}$, while good closure is observed for the method that will be employed on data. Further a closure test was performed where the likelihood was fit to pseudo-experiment and toy data sets corresponding to different nuisance parameter values. The different nuisance parameter values could be extracted with the fit.

In addition, pseudo-experiments are performed with events that are sampled from the simulation samples for different m_t^{gen} values or systematic effects. The estimations of m_t or, respectively, the nuisance parameter corresponding to the simulated systematic effect with the profile likelihood fits are found to be unbiased and to report the correct uncertainty.

5 Results

The results of the profile likelihood fits to data are shown in Fig. 5 (left) for the electron+jets, muon+jets, and lepton+jets channels and the different sets of observables and categories. The observables m_W^{reco} , $m_{\ell b}^{\text{reco}}/m_t^{\text{fit}}$, and R_{bq}^{reco} provide additional constraints on the modeling of the $t\bar{t}$ decays on top of the observables m_t^{fit} and $m_{\ell b}^{\text{reco}}|_{p_{\text{gof}} < 0.2}$ that mainly depend on the m_t value. Figure 6 shows the agreement between the data distribution and the post-fit model. With the profile likelihood method these constraints not only reduce the uncertainty on m_t but also change the measured m_t value as they effectively alter the parameters of the reference $t\bar{t}$ simulation.

When additional observables are included the measurement in the lepton+jets category yields a smaller mass value than the single lepton categories. This is caused by stronger constraints on the nuisance parameters when both lepton channels are combined. With this in mind, the values of m_t are consistent for the different measurements and the 5D result is quoted as the final result.

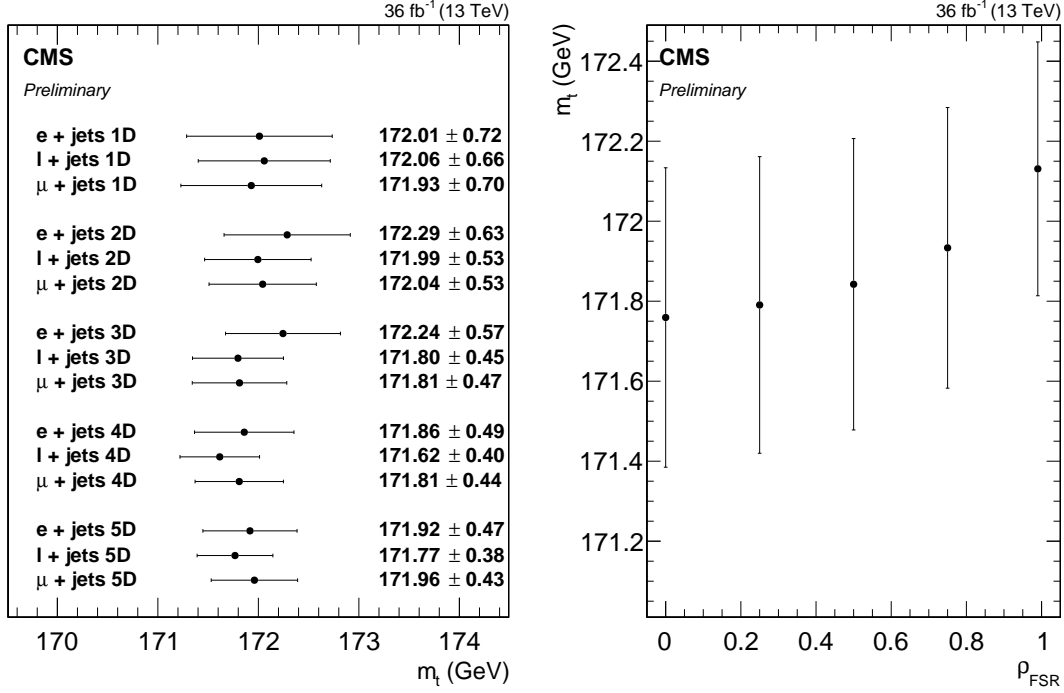


Figure 5: Left: Measurement of m_t in the the three different channels for the different sets of observables and categories. Right: Dependence of the 5D result on the assumed correlation between the FSR PS scales per branching in the lepton + jets channel.

The 5D fit to the selected events yields in the respective channels:

$$\begin{aligned}
 \text{electron+jets: } m_t^{5D} &= 171.92 \pm 0.47 \text{ GeV,} \\
 \text{muon+jets: } m_t^{5D} &= 171.96 \pm 0.43 \text{ GeV,} \\
 \text{lepton+jets: } m_t^{5D} &= 171.77 \pm 0.38 \text{ GeV.}
 \end{aligned}$$

Figure 7 shows the pulls on the most important systematic nuisance parameters θ after the fit and the impacts of the corresponding systematic effect on the uncertainty of the m_t measurement. The impacts are evaluated by repeating the ML fit with the studied nuisance θ fixed to $\hat{\theta} \pm \Delta\theta$, where $\hat{\theta}$ is the value and $\Delta\theta$ the standard deviation of the nuisance parameter after the fit. The impacts are evaluated with the pre- and post-fit values for $\hat{\theta}$ and $\Delta\theta$. If the systematic nuisance parameters θ have *statistical* nuisance parameters ω that account for the statistical uncertainty on the θ -dependence of the model, the corresponding statistical nuisance parameters ω are fixed to their post-fit values in the impact evaluation. In this case, the post-fit impact plotted in Fig. 7 is the combined impact of the systematic and *statistical* nuisance parameters. To estimate it, the likelihood fit is repeated with the corresponding nuisance parameters fixed to their post-fit values and the quadratic difference of the overall m_t uncertainty compared to the default fit is taken. The quadratic difference between the combined impact and the post-

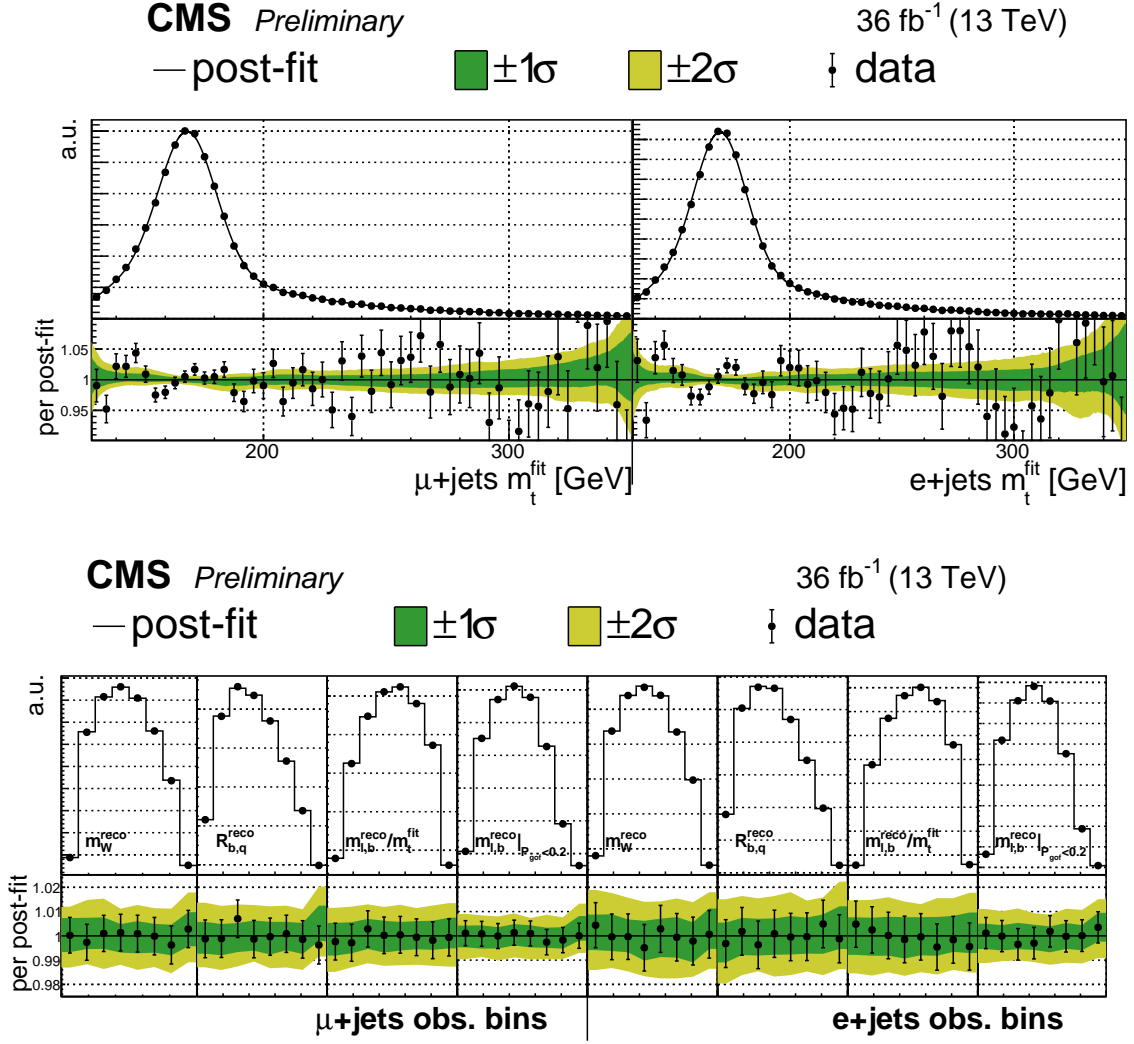


Figure 6: Distribution of m_t^{fit} (top) and the additional observables (bottom) that are the input to the ML fit and their post-fit probability density functions. The green and yellow bands represent the 1-sigma and 2-sigma error bands.

fit impact of only the systematic nuisance is interpreted as the effect of the limited size of the systematic simulation sample.

Most nuisance parameters agree well with their pre-fit values. Many of the nuisance parameters that show a strong post-fit constraint correspond to systematic uncertainties evaluated on independent samples of limited size and are accompanied by additional *statistical* nuisance parameters. A comparison of the pre-fit and post-fit impacts where the post-fit impacts include the impact of these *statistical* nuisance parameters shows that there is hardly a constraint by the fit on the corresponding systematic uncertainties. In addition, the impact of the JER uncertainty is strongly reduced by the fit as the energy resolution of jets from $t\bar{t}$ decays can be measured much better from the width of the m_W^{reco} distribution than by the extrapolation of the resolution measurement with dijet topologies at much higher transverse momenta [40].

The only remaining nuisance with an impact above 0.05 GeV and a strong pull corresponds to the FSR PS scale of the $q \rightarrow qg$ category. The pull is caused by the difference in the peak

CMS Preliminary

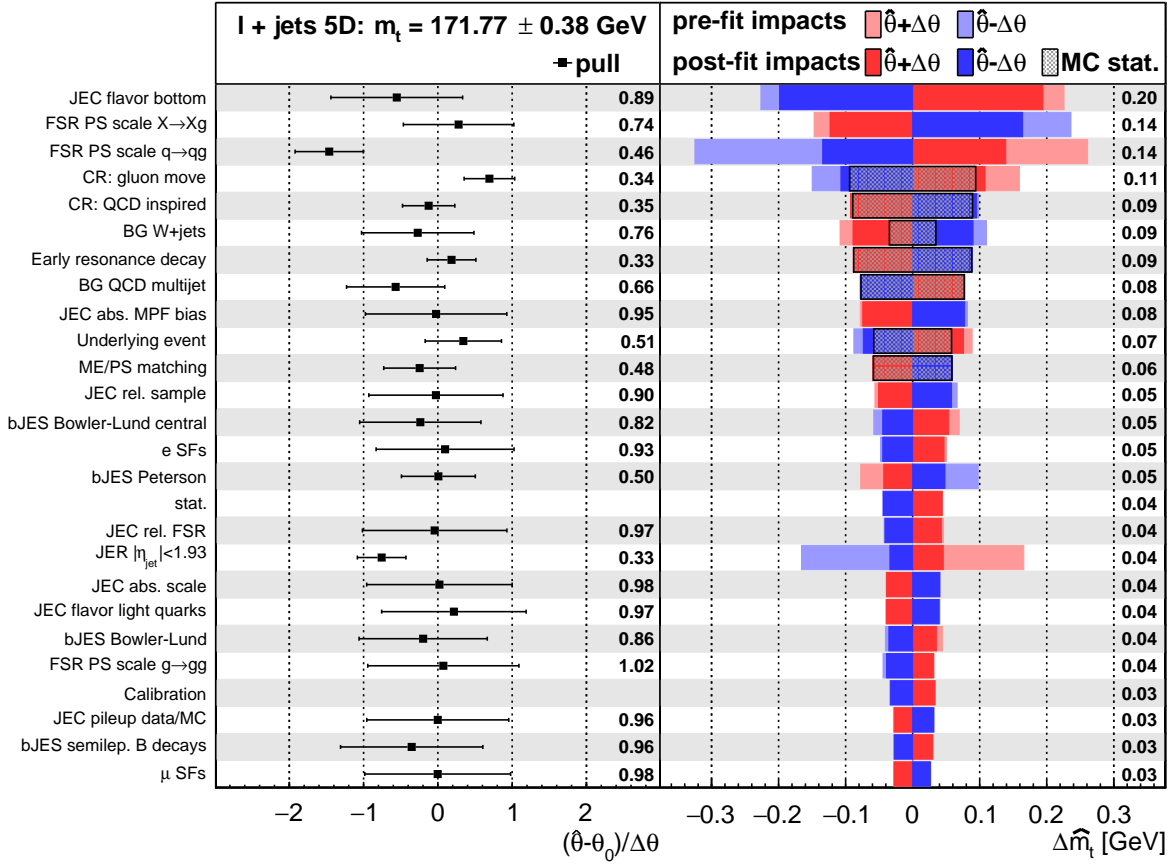
36 fb⁻¹ (13 TeV)

Figure 7: Measurement of m_t in the combined lepton+jets channel using the 5D set of observables and categories. The left plot shows the post-fit pulls on the most important nuisance parameters and the numbers quote the post-fit uncertainty on the nuisance parameter. The right plot shows their pre-fit and post-fit impacts. The post-fit impacts include the contribution from the nuisance parameters accounting for the limited size of simulation samples (MC stat.). The average of these post-fit impacts is printed on the right. The rows are sorted by the size of the post-fit impact.

position of m_W^{reco} seen in Fig. 2 right and the assumption that the FSR PS scale choices for the different FSR categories are uncorrelated. The previous measurements in this channel by CMS assumed correlated FSR PS scales. In that case, a lower peak position in the m_W^{reco} distribution would also cause the m_t^{fit} peak position to be lower than expected from simulation for a given m_t value, resulting in a higher top quark mass value to be measured. In fact, a 5D fit to data assuming fully correlated FSR PS scale choices returns $m_t = 172.14 \pm 0.31$ GeV. This value is in better agreement with the previous measurement on the same data of $m_t = 172.25 \pm 0.08$ (stat+JSF) ± 0.62 (syst) GeV, taking into account the changes in the event reconstruction and selection and in the simulation. The assumption of fully correlated FSR PS scale choices would also reduce the overall uncertainty significantly as parts of the impacts from the scale choice for gluon radiation from b quarks ($X \rightarrow Xg$) and light quarks ($q \rightarrow qg$) cancel each other out. Due to the significant deviation for the FSR PS scale of the $q \rightarrow qg$ branching from the default simulation the final result strongly depends on the choice of the correlation between the FSR PS scales. The measurement is repeated for different correlation coefficients

in the pre-fit covariance matrix between the FSR PS scales for the different branching types. The result of this study is shown in Fig. 5 (right). As there is only a small dependence on FSR PS scale correlations at low correlation coefficients ($\rho_{\text{FSR}} < 0.5$), we stay with the assumption of uncorrelated FSR PS scales per branching for this measurement which is also supported by the difference in the values of the nuisance parameters for the FSR PS scales per branching.

The presented result denotes a considerable improvement compared to all previously published top quark mass measurements. The analysis shows the precision that is achievable from direct measurements of the top quark mass. As the uncertainty on the relation of the direct measurement from simulation templates to a theoretically well defined top quark mass is currently of similar size, the measurement should fuel further theoretical studies on the topic.

6 Summary

The mass of the top quark is measured in 36 fb^{-1} of LHC proton-proton collision data collected with the CMS detector at $\sqrt{s} = 13 \text{ TeV}$. The measurement uses a sample of $t\bar{t}$ events containing one isolated muon or electron and at least four jets in the final state. For each event the mass is reconstructed from a kinematic fit of the decay products to a $t\bar{t}$ hypothesis. A likelihood method is applied to up to five observables to extract the top quark mass and constrain the influence of systematic effects which are included as nuisance parameters in the likelihood. Consistent results are obtained for measurements with different sets of observables and the top quark mass is measured to be $171.77 \pm 0.38 \text{ GeV}$, including 0.04 GeV statistical uncertainty. This result denotes a considerable improvement compared to all previously published top quark mass measurements and supersedes the previously published measurement in this channel on the same data set.

References

- [1] CDF Collaboration, “Observation of top quark production in $\bar{p}p$ collisions”, *Phys. Rev. Lett.* **74** (1995) 2626, doi:10.1103/PhysRevLett.74.2626, arXiv:hep-ex/9503002.
- [2] D0 Collaboration, “Observation of the top quark”, *Phys. Rev. Lett.* **74** (1995) 2632, doi:10.1103/PhysRevLett.74.2632, arXiv:hep-ex/9503003.
- [3] G. Degrandi et al., “Higgs mass and vacuum stability in the standard model at NNLO”, *JHEP* **08** (2012) 1, doi:10.1007/JHEP08(2012)098, arXiv:1205.6497.
- [4] F. Bezrukov, M. Y. Kalmykov, B. A. Kniehl, and M. Shaposhnikov, “Higgs boson mass and new physics”, *JHEP* **10** (2012) 140, doi:10.1007/JHEP10(2012)140, arXiv:1205.2893.
- [5] The ALEPH, CDF, D0, DELPHI, L3, OPAL, SLD Collaborations, the LEP Electroweak Working Group, the Tevatron Electroweak Working Group, and the SLD electroweak and heavy flavour groups, “Precision Electroweak Measurements and Constraints on the Standard Model”, technical report, ALEPH, 2010. arXiv:1012.2367.
- [6] M. Baak et al., “The electroweak fit of the standard model after the discovery of a new boson at the LHC”, *Eur. Phys. J. C* **72** (2012) 2205, doi:10.1140/epjc/s10052-012-2205-9, arXiv:1209.2716.

-
- [7] M. Baak et al., “The global electroweak fit at NNLO and prospects for the LHC and ILC”, *Eur. Phys. J. C* **74** (2014) 3046, doi:10.1140/epjc/s10052-014-3046-5, arXiv:1407.3792.
 - [8] Particle Data Group, P. A. Zyla et al., “Review of particle physics”, *Prog. Theor. Exp. Phys.* **2020** (2020) 083C01, doi:10.1093/ptep/ptaa104.
 - [9] CDF and D0 Collaborations, “Combination of CDF and D0 results on the mass of the top quark using up 9.7 fb^{-1} at the Tevatron”, FERMILAB-CONF-16-298-E, TEVEWWG/top2016/01, arXiv:1608.01881, Fermilab, 2016.
 - [10] ATLAS Collaboration, “Measurement of the top quark mass in the $t\bar{t} \rightarrow \text{lepton} + \text{jets}$ channel from $\sqrt{s} = 8 \text{ TeV}$ ATLAS data and combination with previous results”, *Eur. Phys. J. C* **79** (2019), no. 4, 290, doi:10.1140/epjc/s10052-019-6757-9, arXiv:1810.01772.
 - [11] CMS Collaboration, “Measurement of the top quark mass using proton-proton data at $\sqrt{s} = 7$ and 8 TeV ”, *Phys. Rev. D* **93** (2016) 072004, doi:10.1103/PhysRevD.93.072004, arXiv:1509.04044.
 - [12] A. H. Hoang, “What Is the Top Quark Mass?”, *Ann. Rev. Nucl. Part. Sci.* **70** (2020) 225, doi:10.1146/annurev-nucl-101918-023530, arXiv:2004.12915.
 - [13] CMS Collaboration, “Measurement of the top quark mass with lepton+jets final states using pp collisions at $\sqrt{s} = 13 \text{ TeV}$ ”, *Eur. Phys. J. C* **78** (2018) 891, doi:10.1140/epjc/s10052-018-6332-9, arXiv:1805.01428.
 - [14] DELPHI Collaboration, “Measurement of the mass and width of the W boson in e^+e^- collisions at $\sqrt{s} = 161 - 209 \text{ GeV}$ ”, *Eur. Phys. J. C* **55** (2008) 1, doi:10.1140/epjc/s10052-008-0585-7, arXiv:0803.2534.
 - [15] CMS Collaboration, “Measurement of the top-quark mass in $t\bar{t}$ events with lepton+jets final states in pp collisions at $\sqrt{s} = 7 \text{ TeV}$ ”, *JHEP* **12** (2012) 105, doi:10.1007/JHEP12(2012)105, arXiv:1209.2319.
 - [16] CMS Collaboration, “Extraction and validation of a new set of CMS PYTHIA 8 tunes from underlying-event measurements”, *Eur. Phys. J. C* **80** (2020), no. 1, 4, doi:10.1140/epjc/s10052-019-7499-4, arXiv:1903.12179.
 - [17] E. Bols et al., “Jet flavour classification using DeepJet”, *JINST* **15** (2020), no. 12, P12012, doi:10.1088/1748-0221/15/12/P12012, arXiv:2008.10519.
 - [18] CMS Collaboration, “Precision luminosity measurement in proton-proton collisions at $\sqrt{s} = 13 \text{ TeV}$ in 2015 and 2016 at CMS”, *Eur. Phys. J. C* **81** (2021), no. 9, 800, doi:10.1140/epjc/s10052-021-09538-2, arXiv:2104.01927.
 - [19] CMS Collaboration, “The CMS trigger system”, *JINST* **12** (2017) P01020, doi:10.1088/1748-0221/12/01/P01020, arXiv:1609.02366.
 - [20] P. Nason, “A new method for combining NLO QCD with shower Monte Carlo algorithms”, *JHEP* **11** (2004) 040, doi:10.1088/1126-6708/2004/11/040, arXiv:hep-ph/0409146.

- [21] S. Frixione, P. Nason, and C. Oleari, “Matching NLO QCD computations with parton shower simulations: the POWHEG method”, *JHEP* **11** (2007) 070, doi:10.1088/1126-6708/2007/11/070, arXiv:0709.2092.
- [22] S. Alioli, P. Nason, C. Oleari, and E. Re, “A general framework for implementing NLO calculations in shower Monte Carlo programs: the POWHEG BOX”, *JHEP* **06** (2010) 043, doi:10.1007/JHEP06(2010)043, arXiv:1002.2581.
- [23] T. Sjöstrand, S. Mrenna, and P. Z. Skands, “PYTHIA 6.4 Physics and Manual”, *JHEP* **05** (2006) 026, doi:10.1088/1126-6708/2006/05/026, arXiv:hep-ph/0603175.
- [24] T. Sjöstrand et al., “An introduction to PYTHIA 8.2”, *Comput. Phys. Commun.* **191** (2015) 159, doi:10.1016/j.cpc.2015.01.024, arXiv:1410.3012.
- [25] M. Botje et al., “The PDF4LHC Working Group Interim Recommendations”, arXiv:1101.0538.
- [26] S. Alekhin et al., “The PDF4LHC Working Group Interim Report”, arXiv:1101.0536.
- [27] NNPDF Collaboration, “Parton distributions from high-precision collider data”, *Eur. Phys. J. C* **77** (2017), no. 10, 663, doi:10.1140/epjc/s10052-017-5199-5, arXiv:1706.00428.
- [28] S. Alioli, P. Nason, C. Oleari, and E. Re, “NLO single-top production matched with shower in POWHEG: s - and t -channel contributions”, *JHEP* **09** (2009) 111, doi:10.1088/1126-6708/2009/09/111, arXiv:0907.4076. [Erratum: doi:10.1007/JHEP02(2010)011].
- [29] E. Re, “Single-top Wt -channel production matched with parton showers using the POWHEG method”, *Eur. Phys. J. C* **71** (2011) 1547, doi:10.1140/epjc/s10052-011-1547-z, arXiv:1009.2450.
- [30] J. Alwall et al., “The automated computation of tree-level and next-to-leading order differential cross sections, and their matching to parton shower simulations”, *JHEP* **07** (2014) 079, doi:10.1007/JHEP07(2014)079, arXiv:1405.0301.
- [31] J. Alwall et al., “Comparative study of various algorithms for the merging of parton showers and matrix elements in hadronic collisions”, *Eur. Phys. J. C* **53** (2008) 473, doi:10.1140/epjc/s10052-007-0490-5, arXiv:0706.2569.
- [32] R. Frederix and S. Frixione, “Merging meets matching in MC@NLO”, *JHEP* **12** (2012) 061, doi:10.1007/JHEP12(2012)061, arXiv:1209.6215.
- [33] P. Skands, S. Carrazza, and J. Rojo, “Tuning PYTHIA 8.1: the Monash 2013 Tune”, *Eur. Phys. J. C* **74** (2014) 3024, doi:10.1140/epjc/s10052-014-3024-y, arXiv:1404.5630.
- [34] GEANT4 Collaboration, “GEANT4—a simulation toolkit”, *Nucl. Instrum. Meth. A* **506** (2003) 250, doi:10.1016/S0168-9002(03)01368-8.
- [35] M. Czakon and A. Mitov, “Top++: A program for the calculation of the top-pair cross-section at hadron colliders”, *Comput. Phys. Commun.* **185** (2014) 2930, doi:10.1016/j.cpc.2014.06.021, arXiv:1112.5675.

-
- [36] Y. Li and F. Petriello, “Combining QCD and electroweak corrections to dilepton production in FEWZ”, *Phys. Rev. D* **86** (2012) 094034, doi:10.1103/PhysRevD.86.094034, arXiv:1208.5967.
 - [37] P. Kant et al., “HatHor for single top-quark production: Updated predictions and uncertainty estimates for single top-quark production in hadronic collisions”, *Comput. Phys. Commun.* **191** (2015) 74, doi:10.1016/j.cpc.2015.02.001, arXiv:1406.4403.
 - [38] N. Kidonakis, “NNLL threshold resummation for top-pair and single-top production”, *Phys. Part. Nucl.* **45** (2014) 714, doi:10.1134/S1063779614040091, arXiv:1210.7813.
 - [39] T. Sjöstrand, S. Mrenna, and P. Z. Skands, “A Brief Introduction to PYTHIA 8.1”, *Comput. Phys. Commun.* **178** (2008) 852, doi:10.1016/j.cpc.2008.01.036, arXiv:0710.3820.
 - [40] CMS Collaboration, “Jet energy scale and resolution in the CMS experiment in pp collisions at 8 TeV”, *JINST* **12** (2017) P02014, doi:10.1088/1748-0221/12/02/P02014, arXiv:1607.03663.
 - [41] CMS Collaboration, “Performance of the DeepJet b tagging algorithm using 41.9/fb of data from proton-proton collisions at 13 TeV with Phase 1 CMS detector”, CMS Detector Performance Note CMS-DP-2018-058, CMS, 2018.
 - [42] D0 Collaboration, “Direct measurement of the top quark mass at D0”, *Phys. Rev. D* **58** (1998) 052001, doi:10.1103/PhysRevD.58.052001, arXiv:hep-ex/9801025.
 - [43] ATLAS Collaboration, “Measurement of the top quark mass in the $t\bar{t} \rightarrow$ dilepton channel from $\sqrt{s} = 8$ TeV ATLAS data”, *Phys. Lett. B* **761** (2016) 350, doi:10.1016/j.physletb.2016.08.042, arXiv:1606.02179.
 - [44] CMS Collaboration, “Measurement of the $t\bar{t}$ production cross section, the top quark mass, and the strong coupling constant using dilepton events in pp collisions at $\sqrt{s} = 13$ TeV”, *Eur. Phys. J. C* **79** (2019), no. 5, 368, doi:10.1140/epjc/s10052-019-6863-8, arXiv:1812.10505.
 - [45] ATLAS Collaboration, “Measurement of the top quark mass in the $t\bar{t} \rightarrow$ lepton+jets and $t\bar{t} \rightarrow$ dilepton channels using $\sqrt{s} = 7$ TeV ATLAS data”, *Eur. Phys. J. C* **75** (2015), no. 7, 330, doi:10.1140/epjc/s10052-015-3544-0, arXiv:1503.05427.
 - [46] CMS Collaboration, “Measurement of the top quark mass in the all-jets final state at $\sqrt{s} = 13$ TeV and combination with the lepton+jets channel”, *Eur. Phys. J. C* **79** (2019), no. 4, 313, doi:10.1140/epjc/s10052-019-6788-2, arXiv:1812.10534.
 - [47] CMS Collaboration, “Measurement of the inelastic proton-proton cross section at $\sqrt{s} = 13$ TeV”, *JHEP* **07** (2018) 161, doi:10.1007/JHEP07(2018)161, arXiv:1802.02613.
 - [48] CMS Collaboration, “Measurement of the t-channel single-top-quark production cross section and of the $|V_{tb}|$ CKM matrix element in pp collisions at $\sqrt{s} = 8$ TeV”, *JHEP* **06** (2014) 090, doi:10.1007/JHEP06(2014)090, arXiv:1403.7366.
 - [49] CMS Collaboration, “Cross section measurement of t-channel single top quark production in pp collisions at $\sqrt{s} = 13$ TeV”, *Phys. Lett. B* **772** (2017) 752, doi:10.1016/j.physletb.2017.07.047, arXiv:1610.00678.

- [50] CMS Collaboration, “Measurement of the production cross section of a W boson in association with two b jets in pp collisions at $\sqrt{s} = 8$ TeV”, *Eur. Phys. J. C.* **77** (2017) 92, doi:10.1140/epjc/s10052-016-4573-z, arXiv:1608.07561.
- [51] CMS Collaboration, “Measurements of the associated production of a Z boson and b jets in pp collisions at $\sqrt{s} = 8$ TeV”, *Eur. Phys. J. C* **77** (2017) 751, doi:10.1140/epjc/s10052-017-5140-y, arXiv:1611.06507.
- [52] CMS Collaboration, “Measurement of the WZ production cross section in pp collisions at $\sqrt{s} = 13$ TeV”, *Phys. Lett. B* **766** (2017) 268, doi:10.1016/j.physletb.2017.01.011, arXiv:1607.06943.
- [53] CMS Collaboration, “Measurements of the $pp \rightarrow ZZ$ production cross section and the $Z \rightarrow 4\ell$ branching fraction, and constraints on anomalous triple gauge couplings at $\sqrt{s} = 13$ TeV”, *Eur. Phys. J. C* **78** (2018) 165, doi:10.1140/epjc/s10052-018-5567-9, arXiv:1709.08601.
- [54] M. Bähr et al., “Herwig++ physics and manual”, *Eur. Phys. J. C* **58** (2008) 639, doi:10.1140/epjc/s10052-008-0798-9, arXiv:0803.0883.
- [55] DELPHI Collaboration, “A study of the b-quark fragmentation function with the DELPHI detector at LEP I and an averaged distribution obtained at the Z Pole”, *Eur. Phys. J. C* **71** (2011) 1557, doi:10.1140/epjc/s10052-011-1557-x, arXiv:1102.4748.
- [56] ALEPH Collaboration, “Study of the fragmentation of b quarks into B mesons at the Z peak”, *Phys. Lett. B* **512** (2001) 30, doi:10.1016/S0370-2693(01)00690-6, arXiv:hep-ex/0106051.
- [57] S. Dulat et al., “New parton distribution functions from a global analysis of quantum chromodynamics”, *Phys. Rev. D* **93** (2016), no. 3, 033006, doi:10.1103/PhysRevD.93.033006, arXiv:1506.07443.
- [58] L. A. Harland-Lang, A. D. Martin, P. Motylinski, and R. S. Thorne, “Parton distributions in the LHC era: MMHT 2014 PDFs”, *Eur. Phys. J. C* **75** (2015), no. 5, 204, doi:10.1140/epjc/s10052-015-3397-6, arXiv:1412.3989.
- [59] CMS Collaboration, “Investigations of the impact of the parton shower tuning in PYTHIA 8 in the modelling of $t\bar{t}$ at $\sqrt{s} = 8$ and 13 TeV”, CMS Physics Analysis Summary CMS-PAS-TOP-16-021, CMS, 2016.
- [60] S. Mrenna and P. Skands, “Automated Parton-Shower Variations in Pythia 8”, *Phys. Rev. D* **94** (2016), no. 7, 074005, doi:10.1103/PhysRevD.94.074005, arXiv:1605.08352.
- [61] M. Czakon, D. Heymes, and A. Mitov, “High-precision differential predictions for top-quark pairs at the LHC”, *Phys. Rev. Lett.* **116** (2016) 082003, doi:10.1103/PhysRevLett.116.082003, arXiv:1511.00549.
- [62] M. Czakon et al., “Top-pair production at the LHC through NNLO QCD and NLO EW”, *JHEP* **10** (2017) 186, doi:10.1007/JHEP10(2017)186, arXiv:1705.04105.
- [63] S. Catani et al., “Top-quark pair production at the LHC: Fully differential QCD predictions at NNLO”, *JHEP* **07** (2019) 100, doi:10.1007/JHEP07(2019)100, arXiv:1906.06535.

- [64] CMS Collaboration, “Measurement of differential cross sections for top quark pair production using the lepton+jets final state in proton-proton collisions at 13 TeV”, *Phys. Rev. D* **95** (2017) 092001, doi:10.1103/PhysRevD.95.092001, arXiv:1610.04191.
- [65] CMS Collaboration, “Measurement of normalized differential $t\bar{t}$ cross sections in the dilepton channel from pp collisions at $\sqrt{s} = 13$ TeV”, *JHEP* **04** (2018) 060, doi:10.1007/JHEP04(2018)060, arXiv:1708.07638.
- [66] J. R. Christiansen and P. Z. Skands, “String formation beyond leading colour”, *JHEP* **08** (2015) 003, doi:10.1007/JHEP08(2015)003, arXiv:1505.01681.
- [67] S. Argyropoulos and T. Sjöstrand, “Effects of color reconnection on $t\bar{t}$ final states at the LHC”, *JHEP* **11** (2014) 043, doi:10.1007/JHEP11(2014)043, arXiv:1407.6653.
- [68] W. Verkerke and D. P. Kirkby, “The RooFit toolkit for data modeling”, *eConf* **C0303241** (2003) MOLT007, arXiv:physics/0306116.
- [69] F. James and M. Roos, “Minuit: A System for Function Minimization and Analysis of the Parameter Errors and Correlations”, *Comput. Phys. Commun.* **10** (1975) 343, doi:10.1016/0010-4655(75)90039-9.
- [70] P. K. Suetin, “Chebyshev polynomials”. Springer-Verlag, 2002.
http://encyclopediaofmath.org/index.php?title=Chebyshev_polynomials&oldid=16283.